JGR Oceans

RESEARCH ARTICLE
10.1029/2020JC016488

Coupling of the Surface and Near-Bottom Currents in the Gulf of Mexico

Yingli Zhu[1] **and Xinfeng Liang**[1]

[1]School of Marine Science and Policy, University of Delaware, Newark, DE, USA

Key Points:
- Surface and bottom currents in the Gulf of Mexico can be coupled locally by baroclinic instability and remotely by topographic Rossby waves
- Fluctuations generated along the Loop Current have stronger deep ocean expressions at the period of 30–90 days than at longer periods
- Surface and bottom coupling in the Gulf of Mexico varies geographically and is modulated by the Loop Current and the Loop Current eddies

Correspondence to:
Y. Zhu,
yzhu@udel.edu

Citation:
Zhu, Y., & Liang, X. (2020). Coupling of the surface and near-bottom currents in the Gulf of Mexico. *Journal of Geophysical Research: Oceans*, *125*, e2020JC016488. https://doi.org/10.1029/2020JC016488

Received 7 JUN 2020
Accepted 17 OCT 2020
Accepted article online 26 OCT 2020

Abstract Coupling between the surface and near-bottom currents in the Gulf of Mexico (GoM) has been reported in many case studies. However, geographical variations of this coupling need more examination. In this study, surface geostrophic currents derived from satellite-observed sea surface height and subsurface currents from a collection of deep ocean moorings are used to examine the surface and bottom coupling in different parts of the GoM. The short-period (30–90 days) fluctuations generated by the Loop Current (LC) and the LC eddies (LCEs) have a more vertically coherent structure and stronger deep ocean expressions than the long-period fluctuations (>90 days). In addition, the strength of the coupling is modulated by the long-period variations of the LC and LCE sheddings. Moreover, the surface and bottom coupling varies geographically. In the LC region, the surface fluctuations along the eastern side of the LC are important in causing the bottom current fluctuations through baroclinic instability under the LC and through traveling topographic Rossby waves (TRWs) north of the LC. In the central deep GoM, the bottom currents are affected by the upper fluctuations of the northern LC through both local baroclinic instability and remote TRW propagation. In the northwestern GoM, the bottom current fluctuations are largely related to the remote surface variability from the west side of the LC by TRWs propagating northwestward. This study will help us better understand mechanisms of the bottom current fluctuations that are important for the dispersal of deep ocean materials and properties.

Plain Language Summary Bottom currents in the Gulf of Mexico (GoM) are important in many ways, such as transporting fish larvae and spilled oil. However, in contrast to surface currents that are easily derived from the abundant satellite observations, our understanding of the bottom currents is very limited. In this study, the relationships between surface and near-bottom current fluctuations in different parts of the GoM are investigated by combining a collection of historical near-bottom current measurements and satellite data. The results show that the bottom current variability is linked to local processes such as current instability or remote processes through planetary wave propagation. The surface and bottom coupling is mainly related to the short-period variability generated along the Loop Current and the Loop Current eddies and has a significant influence on the bottom currents. Although the long-period fluctuations have weak bottom expressions, they can modulate the strength of the short-period coupling. Studying the coupling between the surface and bottom current fluctuations in the GoM can advance our understanding of mechanisms of the bottom currents that are important for the deep ocean ecosystem and industrial operations.

1. Introduction

The ocean circulation in the Gulf of Mexico (GoM) is not vertically coherent through the water column. Typically, the circulation in the GoM is characterized by two layers, the stratified upper layer (above 800–12,00 m) with surface-intensified currents and the weakly stratified lower layer (below 800–1,200 m) with vertically coherent currents (e.g., Hamilton, 1990). The surface and upper-layer oceans have been widely investigated with hydrographic, drifter, mooring, and satellite observations, especially with sea surface height (SSH) observations from satellite altimeters. Major upper-layer features, such as the Loop Current (LC) and the Loop Current eddies (LCEs), have been described in detail (e.g., Alvera-Azcárate et al., 2009; DiMarco et al., 2005; Elliott, 1982; Leben, 2005; Schmitz, 2005; Sturges & Leben, 2000; Vukovich, 1995; Weisberg & Liu, 2017). In the vertical direction, the LC and the LCEs can extend to 800–1,000 m, where the weakest currents are usually observed (Hamilton et al., 2000). Below that level, limited observations from mooring arrays and deep ocean floats indicate that the current variability in the lower layer is largely from mesoscale eddies

and topographic Rossby waves (TRWs) (e.g., Furey et al., 2018; Hamilton, 1990; Kolodziejczyk et al., 2011; Tenreiro et al., 2018), which are nearly depth independent or bottom intensified in the deep layer. Also, because group speeds of the TRWs are faster than the LCE propagation speeds, deep ocean motions become progressively decoupled from those in the upper layer from east to west (Hamilton, 1990).

Case studies of the coupling between the upper and lower layers show linkages between the LC and the LCEs and the deep ocean eddies over particular periods and locations (e.g., Donohue et al., 2008, 2016; Inoue et al., 2008). For instance, when the LC extends northward or the LCEs travel to the western GoM, surface and deep ocean coupling is detected from mooring observations (e.g., Tenreiro et al., 2018; Welsh et al., 2009). Model studies also show that deep currents can be related to the LC or the LCEs (e.g., Chérubin et al., 2005; Oey et al., 2009; Romanou et al., 2004; Sturges et al., 1993; Welsh & Inoue, 2000; Welsh et al., 2009). For example, Lee and Mellor (2003) show that the LC can spin up a deep cyclonic circulation that varies with the southward current of the eastern limb of the LC and anticyclonic lower-layer eddies with a larger propagation speed, leading the surface rings into the central GoM. It is also found that short-scale fluctuations along the LC and the LCEs have more profound impacts on the lower-layer motions than the long-period LC variations and LCE sheddings (Oey & Lee, 2002) that affect the deep ocean currents at the time scale of months (Chang & Oey, 2011).

A variety of mechanisms for the upper- and lower-layer coupling have been proposed. One mechanism proposed by Cushman-Roisin et al. (1990) depicts that as one upper-layer eddy travels westward over a flat bottom, a pair of eddies in the lower layer is generated ahead and behind the surface-intensified eddy, resulting from potential vorticity conservation. It is implied that this mechanism is responsible for the coupling in the western GoM (Tenreiro et al., 2018). Moreover, other observational as well as numerical studies highlight the importance of both barotropic and baroclinic instability of the LC, the LCEs, and the LC front eddies (LCFEs) in the generation of lower-layer cyclones and anticyclones (Chérubin et al., 2006; Donohue et al., 2016; Hamilton, Bower, et al., 2016; Hamilton et al., 2019; Hamilton, Lugo-Fernández, et al., 2016; Hurlburt & Thompson, 1980; Oey, 1996, 2008; Xu et al., 2013). Atmospheric forcing (Welsh & Inoue, 2000) and topography are important factors in influencing the dynamics in the deep ocean as well (Cardona & Bracco, 2016; Donohue et al., 2008; Frolov et al., 2004; LaCasce, 1998). Overall, short-period near-bottom motions at the source regions derive their energy from short-period (<100 days) upper-ocean fluctuations such as the LC meanders along the northward extruding LC, while long-period (>100 days) fluctuations are associated with the large-scale variations of the LC and the LCE sheddings (Hamilton et al., 2014; Oey & Lee, 2002).

Although occasional connections between surface and bottom currents have been reported in the case studies aforementioned, it is unclear whether these events are statistically significant (Hamilton, 2007), whether some regions in the GoM facilitate the coupling, and whether the surface regime responsible for the coupling varies geographically. Various programs in the deep GoM have been conducted (e.g., Donohue et al., 2006, 2008; Hamilton et al., 2000, 2003, 2014; McKone et al., 2007; Welsh et al., 2009). However, mooring arrays in each research program are limited by their spatial coverage, and the Lagrangian floats in the deep GoM are not continuous in time at one fixed location despite their large spatial coverage. A collection of deep ocean current data from various observational programs can provide a relatively large spatial coverage (Hamilton, 2009).

In an attempt to examine the surface and near-bottom ocean coupling in different regions of the GoM, we collected available current records near the ocean bottom from a number of previous research programs and combined them with the surface currents derived from satellite-observed SSH. Representative cases for three regions in the GoM are presented. Both local coupling processes such as baroclinic instability and remote processes that involve TRW propagation are described. This paper is organized as follows. Section 2 presents data including ocean currents from historical observations and one GoM ocean reanalysis data set. Section 3 describes the coupling cases in the LC region, the central GoM, and the northwestern GoM. The major conclusions are presented, and the coupling pattern in the GoM is also discussed in section 4.

2. Data

Gridded SSH observations from multimission altimeter satellites provided by Copernicus Marine Environment Monitoring Service (CMEMS) were used for the surface current calculation. This SSH data set is produced by optimal interpolation of along-track SSH anomalies from satellite altimeters from 1993 to

Table 1
Mooring Arrays in Nine Research Programs

Program (Reference)	Region	Period	Mooring number (Mooring names)
DeSoto Canyon Eddy Intrusion Study[a] (Hamilton et al., 2000)	Northeastern GoM	March 1997 to April 1999	2
Deepwater Observations in the Northern GoM from In Situ Current Meters and PIES[a] (Hamilton et al., 2003)	Sigsbee Escarpment	August 1999 to September 2001	4
Physical Oceanographic Time Series Data from Louisiana State University[a] (McKone et al., 2007)	Northern GoM	February 2000 to October 2004	2
Observation of the Deepwater Manifestation of the Loop Current and Loop Current Rings in the Eastern GoM[a] (Welsh et al., 2009)	Eastern GoM	May 2000 to July 2007	5 (L7)
Exploratory Study of Deepwater Currents in the Northern GoM[a] (Donohue et al., 2006)	Northern GoM	February 2003 to April 2004	15 (O1, O2, Q2, L3, M2, M4)
Northwest GoM Study[a] (Donohue et al., 2008)	Northwestern GoM	March 2004 to July 2005	13 (V3, V4, W3)
Dynamics of the Loop Current[b] (Hamilton et al., 2014)	Eastern GoM	April 2009 to November 2011	14 (D2, D3, D4, D5, D7)
GoM Integrated Spill Response Consortium[c] (DiMarco, 2014)	Northern GoM	July 2012 to July 2013	5
GoM Integrated Spill Response Consortium[c] (DiMarco, 2016)	Northern GoM	July 2013 to July 2014	4

[a]Funded by the U.S. Department of the Interior, Minerals Management Service. [b]Funded by the U.S. Department of the Interior, Bureau of Ocean Energy Management. [c]Funded by the Gulf of Mexico Research Initiative.

present and has a daily time interval and a spatial resolution of 0.25° (Pujol et al., 2016). Mean dynamic topography over 1993–2012 with a spatial resolution of 0.25° distributed by Archiving, Validation, and Interpretation of Satellite Oceanographic (AVISO) was added to the SSH anomalies to obtain the absolute dynamic heights. Surface geostrophic currents were then calculated from SSH observations through geostrophic balance.

Subsurface current data from nine programs carried out after 1993 were collected from the Gulf of Mexico Research Initiative Information and Data Cooperative (GRIIDC) and the National Oceanic and Atmospheric Administration (NOAA) National Centers for Environmental Information (NCEI). Current instruments that were utilized include Acoustic Doppler Current Profilers (ADCPs) and single-point recording current meters (RCMs). Most of the collected data were quality controlled. However, visual inspections of those data still identified abnormal spikes at the beginning or end of some time series. We further processed the selected current data. Zonal or meridional velocities larger than eight standard deviations of each record were removed. Strong currents greater than 1.2 m s^{-1} are rare in the deep ocean and are likely due to instrument errors. We therefore did not include the records that had maximum zonal or meridional velocity larger than 1.2 m s^{-1} below 1,000 m. In order to have complete records that were long enough for spectral and correlation analysis, records with completeness less than 90% or with data length less than 300 days were not selected. The time steps of the selected moored velocity data range from 0.5 to 4.5 hr. The moored velocity data were further low-pass filtered with a cutoff period of 3 days and interpolated into daily data. In this study, near-bottom currents that we focused on were at more than 1,000 m below surface and less than 200 m above bottom.

Observation period, region, number of selected moorings from the nine selected programs, and their references are listed in Table 1. A total of 64 moorings was located over the northern and the eastern GoM during different time periods between 1997 and 2014, while none were found over the southwestern GoM from GRIIDC and NOAA/NCEI. It should be noted that there were deepwater moorings in the western and southwestern GoM (Tenreiro et al., 2018), but they were not accessible at the time of this study. To understand how the coupling varied geographically, the selected moorings were further divided into four groups based on their geographic locations: the LC group around the mean position of the LC, the northeastern group in the northeastern GoM, the central group in the central northern GoM, and the northwestern group in the northwestern GoM (Figure 1). In addition, details of three full-depth moorings are listed in Table 2.

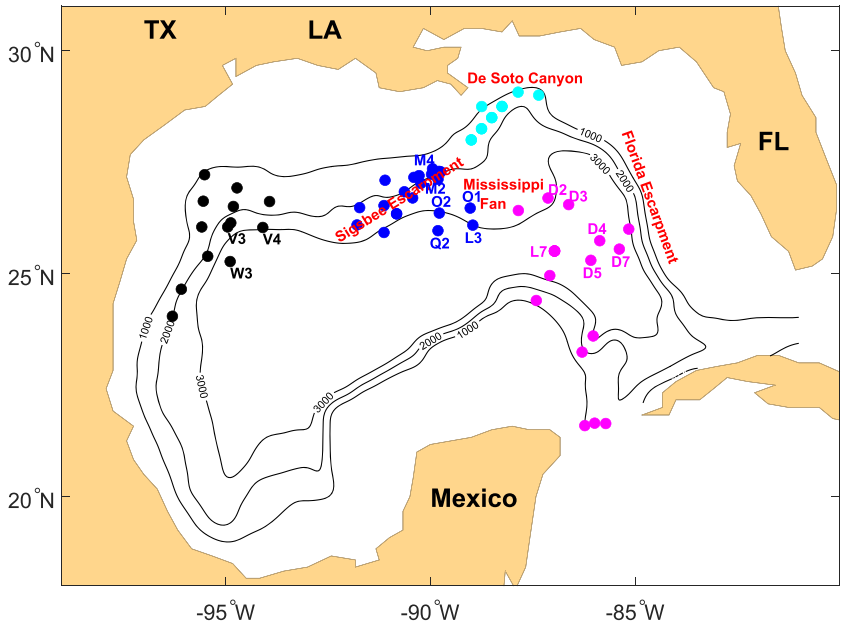

Figure 1. Locations of the collected moorings. Four groups of mooring are marked in different colors, with the LC ones in magenta, the northeastern ones in cyan, the central ones in blue, and the northwestern ones in black. Moorings mentioned in the case studies are labeled with their names. Contours represent 1,000-, 2,000-, and 3,000-m isobaths.

Vertical profiles of temperature from two inverted echo sounders with pressure gauges (PIES) deployed in the central northern GoM between March 2003 and April 2004 (Donohue et al., 2006) were also used to examine the vertical structure of mesoscale variability in that region. The PIES is an instrument that is bottom mounted and emits 12-kHz sound pulses to measure the travel time from the sea floor to the sea surface. Temperature and salinity were derived from hydrographic data and travel times.

Since the gridded SSH observations are produced by an optimal mapping method with temporal correlation scales between 25 and 30 days in the GoM (Pujol et al., 2016), the surface currents derived from SSH observations may not resolve the current variability at periods below 30 days. To examine the real temporal resolution of surface currents derived from the CMEMS SSH product, the spectra of surface currents derived from SSH observations and observed by the moorings were compared with an example shown at mooring L7 (Figure 2a). Compared to the near-surface currents observed by the mooring, the SSH-derived currents show

Table 2
Current Instruments of Three Full-Depth Moorings Denoted in Figure 1

Mooring name (reference)	Instrument depth (m)	Instrument type
L7 (McKone et al., 2007)	140	Upward looking 300 kHz ADCP (11 bins)
	3,190	Downward looking 300 kHz ADCP (15 bins)
	250, 350, 450, 600, 750, 875, 1,001, 1,200, 1,500, 2,000, 2,500, 3,000, 3,186	RCM
L3 (Donohue et al., 2006)	400	Upward looking 75 kHz ADCP (42 bins)
	750, 1,000, 1,500, 2,000, 2,500, 2,900	RCM
V4 (Donohue et al., 2008)	450	Upward looking 75 kHz ADCP (49 bins)
	750, 1,000, 1,500, 2,000, 2,500, 3,000	RCM

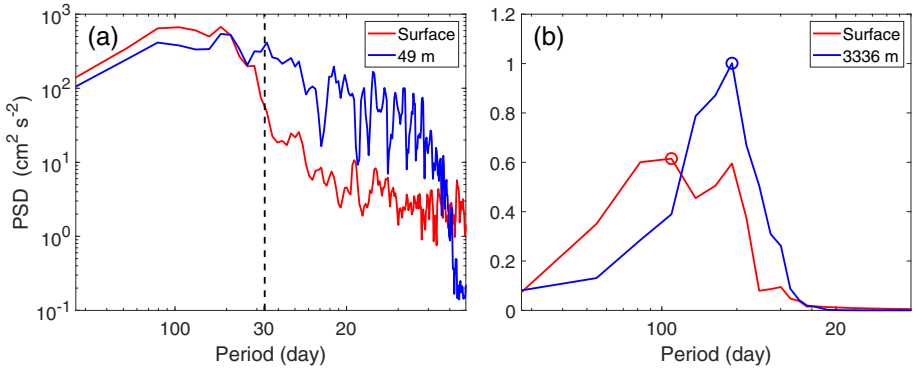

Figure 2. Variance-preserving spectra of the zonal velocities at mooring L7. (a) Spectra of the daily velocities at the surface derived from SSH observations (red) and at 49 m observed by the mooring (blue). The vertical dashed line marks the period of 30 days. (b) Spectra of the velocity low-pass filtered with a cutoff period of 30 days at the surface (red) and at 3,336 m (blue). The peak spectra are denoted by circles.

a dramatic energy reduction at periods shorter than 30 days, which is consistent with the designed temporal correlation scales used to produce the CMEMS SSH field. In this study, to obtain the relationship of the surface and bottom currents on the time scale resolvable in all data sets, all current data were low-pass filtered with a half-amplitude period of 30 days. The low-pass filtering removed the relatively high-frequency current variability observed by moorings, so the energetic deep ocean current variability with periods shorter than 30 days (e.g., Hamilton, 2007, 2009) was not considered in this study.

Energy distribution is different in the filtered surface and bottom currents. The spectra at mooring L7 (Figure 2b) indicate that the surface current energy has a peak at 92 days, which is much longer than that for the bottom currents. The periods with the maximum variance-preserving spectra (T_{max}) for the surface and bottom velocity components were then calculated for all moorings (Figure 3). In general, the current energy near the bottom is concentrated at periods shorter than 90 days, while the current energy at the surface is concentrated at periods longer than those of the currents near the bottom. The discrepancy of the dominant periods of the surface and near-bottom currents is consistent with previous studies (e.g., Hamilton, Lugo-Fernández, et al., 2016; Hamilton et al., 2014). Because the peak current energy in the bottom ocean is distributed around 60 days on average and the current records are not long enough for statistical analysis of the long-period variability, we will focus on the potential coupling in the period band of 30 to 90 days. Both the surface and subsurface currents were band-pass filtered to remove signals with periods shorter than 30 days or longer than 90 days.

Since the correlation analyses from yearlong observations are not fully convincing, Hybrid Coordinate Ocean Model (HYCOM) GOMu0.04 Reanalysis (expt_50.1) data were also used to calculate correlations for comparison in the discussion section. Multiple types of observations such as altimeter observations were

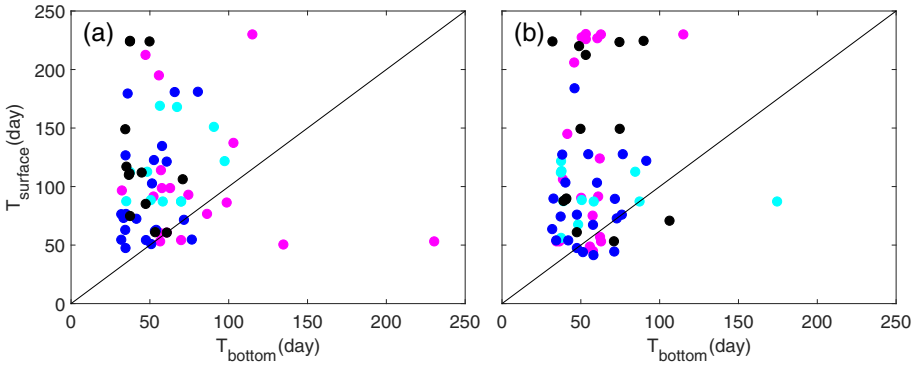

Figure 3. Scatter plots of the periods (day) with peak variance-preserving spectra at the surface versus those in the bottom for the zonal (a) and meridional (b) velocities. Variance-preserving spectra have been smoothed with a 3-point moving average. Four groups of mooring are marked in different colors, with the LC ones in magenta, the northeastern ones in cyan, the central ones in blue, and the northwestern ones in black. The straight line is 1:1 line.

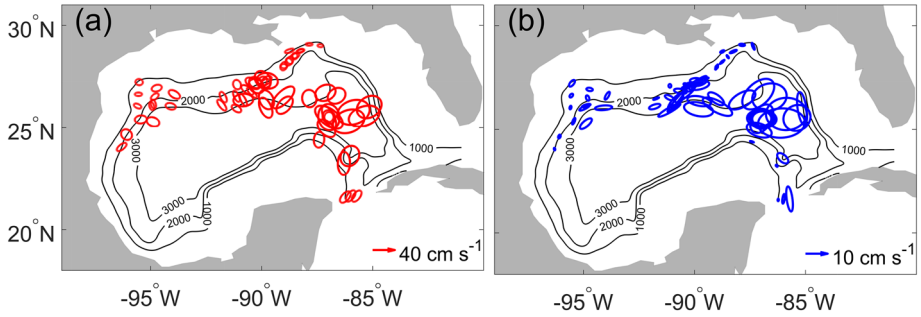

Figure 4. Standard deviation ellipses for the surface currents in red (a) and for the near-bottom currents in blue (b) in the period band of 30 to 90 days. The major and minor axes represent the standard deviations of the two principle components. Black contours represent 1,000-, 2,000-, and 3,000-m isobaths.

assimilated using the Navy Coupled Ocean Data Assimilation (NCODA) system (Cummings, 2005). HYCOM was shown to be able to represent dominant features of the deep circulation in the GoM but with less eddy kinetic energy (EKE) than that computed from observations under the LC (Morey et al., 2020). Daily currents from 2000 to 2010 were chosen with currents at the 100-m level representing surface currents and those near the bottom representing bottom currents. The same band-pass filter was applied to the reanalysis data to obtain the fluctuations in the period band of 30 to 90 days.

The GoM bathymetry data distributed by GRIIDC (Panagiotis, 2014) were used for TRW ray tracing. The ray tracing method assumes that the wave amplitude caused by the environment changes slowly. To apply this method, the environmental parameters including water depth and bottom slope should vary on scales larger than the local TRW wavelength (e.g., Hamilton, 2009). The topography therefore was smoothed with a cutoff wavelength of 100 km for the calculation of environmental variables, such as topographic gradients.

3. Results

Previous studies revealed strong variability in both surface and deep ocean currents around the LC and weak variability in the rest of the GoM (e.g., Liu et al., 2016; Pérez-Brunius et al., 2018). During the periods of the selected mooring observations, the magnitudes of surface and near-bottom currents in the period band of 30 to 90 days show a similar spatial pattern (Figure 4). The standard deviation ellipse provides not only the magnitude but also the direction along which the variance is maximized (Thomson & Emery, 2014). Strong variability appears in the southeastern and the central GoM, where the LC intrudes northwestward frequently and sheds eddies, whereas the northwestern and the northeastern GoM exhibit weak variability. The standard deviation ellipses also show that the surface currents are more isotropic than the near-bottom currents. The surface currents can have a large cross-isobath component even over the steep continent slope, while the major variability of the near-bottom currents tends to follow the topography tendency, indicating an important role of the topography.

We first examined the local coupling between the surface and near-bottom currents at each mooring by calculating the vector correlations (Crosby et al., 1993). The vector correlation is defined such that the correlation is perfect in cases where two vector sequences are linearly dependent and zero in cases where two vectors are independent. Maximum lagged correlations with a maximum temporal lag of 20 days were calculated and shown in Figure 5. To estimate the correlation significance level, the effective degree of freedom (DOF) of velocity was calculated from the velocity autocorrelation function (Thomson & Emery, 2014). Since the low-pass filter removed signals shorter than 30 days, the maximum DOF was set to be the record length divided by 30. The significance level was estimated, assuming that the squared vector correlation times DOF follows a chi square distribution with 4 DOF (Crosby et al., 1993). Most of the correlations are not significant at the 95% confidence level except at moorings D4, D5 in the eastern GoM and Q2 in the central GoM (Figure 5a). Some relatively high correlations though not significant are found in the deep eastern GoM and the upper northern continent slope. It is likely that a mix of locally and remotely generated current fluctuations in the deep ocean could obscure the upper- and lower-layer coupling, resulting in nonsignificant correlations.

To investigate the local and remote coupling processes in more details, some moorings were selected from the LC region, the central northern GoM, and the northwestern GoM (Figure 1). Since the current variability

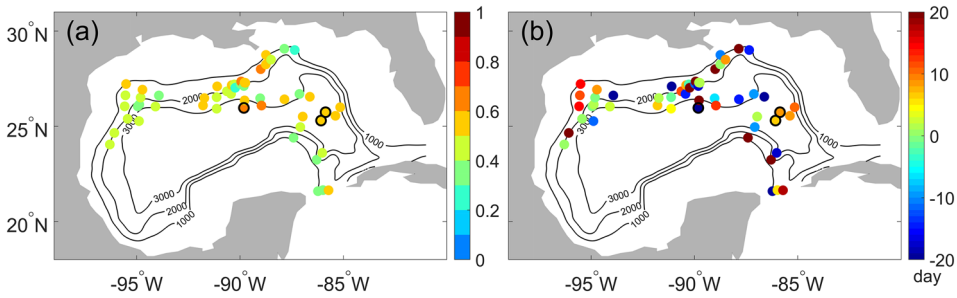

Figure 5. (a) Maximum lagged vector correlation between the surface and near-bottom currents at each mooring. The correlations are normalized to range from 0 to 1, and those significant at the 95% confidence level are enclosed by black circles. (b) Time lags corresponding to the maximum correlations. Negative (positive) lag means surface fluctuations leading (lagging) near-bottom currents. Black contours represent 1,000-, 2,000-, and 3,000-m isobaths.

in the northeastern GoM was so weak during the observation period (Figure 4), this mooring group was not considered in the following study. Also, note that we focused on the coupling in the period band of 30 to 90 days over the three regions.

3.1. The LC Region

In the eastern GoM, moorings in the deep ocean show relatively high vector correlations with two of them being significant (Figure 5a). The associated positive lags of about 10 days (Figure 5b) mean that the deep current fluctuations led those at the surface. Eddies or meanders propagated in the direction of the strong upper-layer LC (Donohue et al., 2016; Hamilton et al., 2014). Along the direction of eddy propagation, a vertical phase tilt with the deep currents leading the upper currents would favor baroclinic instability to transfer energy from the surface to bottom. This kind of local coupling process through baroclinic instability may lead to a correspondence between the surface and bottom EKE within the same water column.

EKE calculated from the 30- to 90-day velocities at the surface and the bottom level (3,211 m) of mooring D4 in the deep eastern GoM shows that the bottom EKE was intensified when the surface EKE increased over three periods, June to October 2009, April to September 2010, and March to July 2011 (Figure 6a). The three periods correspond to three LC eddy shedding events that were reported in detail by Donohue et al. (2016) and Hamilton et al. (2014). During the three LCE shedding periods, the LC intruded northwestward and was in an unstable state with energetic mesoscale perturbations generated along the eastern rim of the LC (Figure 6c). Moorings D4, D5, and D7 were within the high-EKE area during those periods. After the separation of the LCE, the LC retracted to the south and was in a stable state without energetic mesoscale perturbations generated (Figure 6d). Since less surface energy could be transferred into the bottom, the bottom EKE was at a low level. The results agree with a previous modeling study (Oey, 2008) that the surface and deep ocean cyclones amplify together through baroclinic instability, which has been shown to be the dominant mode of the upper-to-deep variability near the LC.

To further examine the mesoscale variability through the water column, the vertical structure of observed currents from a full-depth mooring (L7) deployed in the LC region is shown in Figure 7. Although it was deployed at a different time, between June 2005 and May 2006 (Welsh et al., 2009), it was in the eastern LC where the northwestward intruding LC tended to shed LCEs (not shown). During the observation period, the LC kept deforming in an unstable state with two LCEs shed and energetic mesoscale variability generated along the rim of the LC. The long-period (>90 days) currents showed a surface-intensified structure with a weak expression below 1,000 m (Figure 7a). Compared to the long-period currents, the 30- to 90-day currents had a different vertical structure that perturbations were more coherent through the water column and displayed a stronger bottom expression over most of the observation period. These cases agree with the previous modeling studies that long-period variations of the LC and the LCEs had little direct signature in the lower layer, but short-scale fluctuations generated by them had a profound impact on the lower-layer motions (Oey & Lee, 2002; Xu et al., 2013). Between September 2005 and January 2006, the bottom zonal velocities led that at the surface by about 10 days. As mesoscale perturbations propagated in the direction of the surface-intensified LC, a vertical phase tilt with the bottom currents leading the surface currents was favorable for baroclinic instability. The surface and bottom currents were not always phase locked. At other

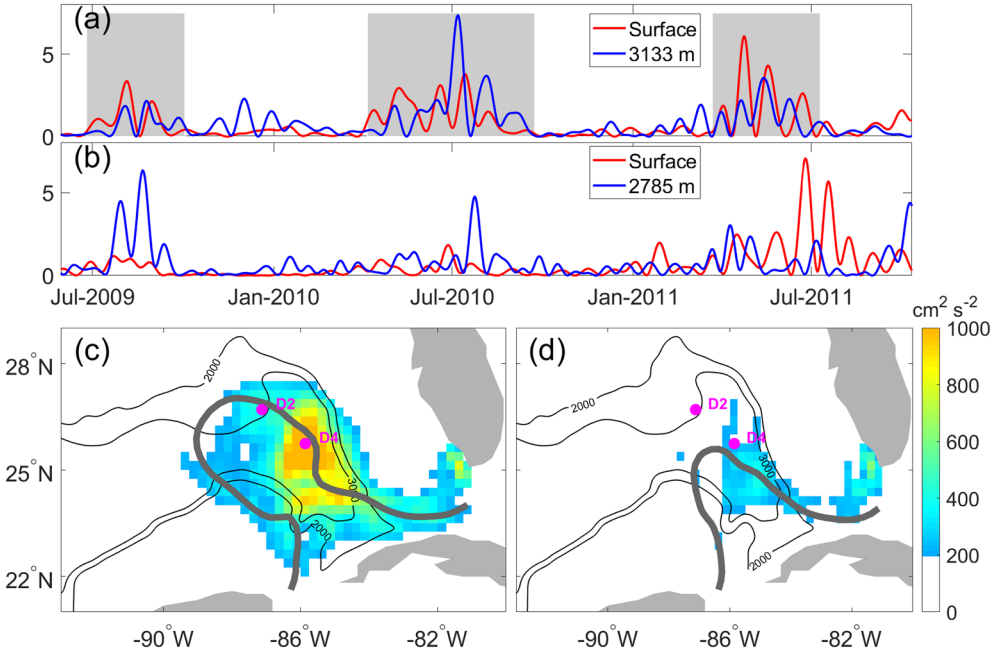

Figure 6. (a) EKE at the surface (red) and a bottom level (blue) at mooring D4 normalized by their standard deviations, 943.4 and 87.5 cm^2 s^{-2}, respectively. Three periods with relatively large EKE are shaded in gray. (b) Surface (red) and bottom (blue) EKE at mooring D2 normalized by their standard deviations, 469.4 and 67 cm^2 s^{-2}, respectively. (c) Mean surface EKE (cm^2 s^{-2}, colored image) and mean SSH at 450 mm (thick gray contour) during the three shaded periods shown in (a). (d) Mean surface EKE and mean SSH at 450 mm at times with small EKE during the observation period at D4. Black contours represent 2,000- and 3,000-m isobaths.

times such as before September 2005, the bottom motions could lag those at the surface by a few days. One possible reason is the different propagation speeds of surface and bottom motions.

A similar structure with occasional vertical coherence has been observed and associated with cyclones and anticyclones generated along the LC (Inoue et al., 2008; Kolodziejczyk et al., 2012). In addition, the vertical structure of velocities with more barotropic flows was also observed in the South China Sea and was explained by a barotropization process in which the baroclinic kinetic energy (KE) was converted to the barotropic KE (Sun et al., 2020). Similarly, the barotropization process might contribute to the coupling in the period band of 30 to 90 days in the LC region too. However, more full-depth mooring observations in the deep LC region are needed to verify the KE conversion between the baroclinic and barotropic flows.

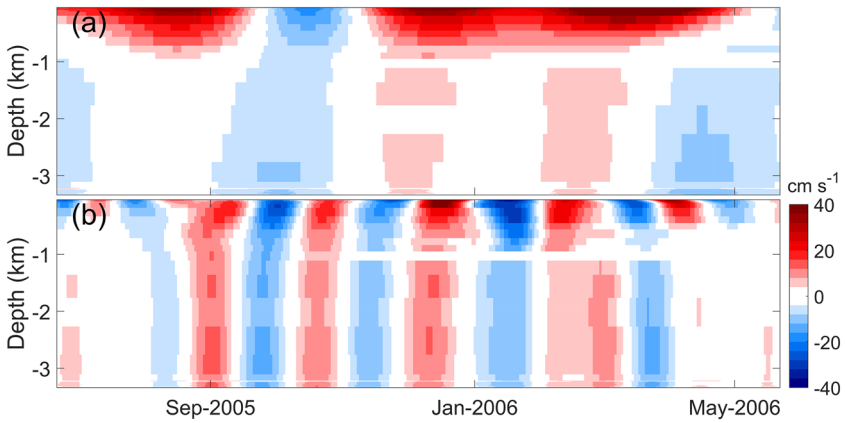

Figure 7. Depth-time section of the zonal velocities (cm s^{-1}) at mooring L7 for the periods longer than 90 days (a) and for the period band of 30 to 90 days (b).

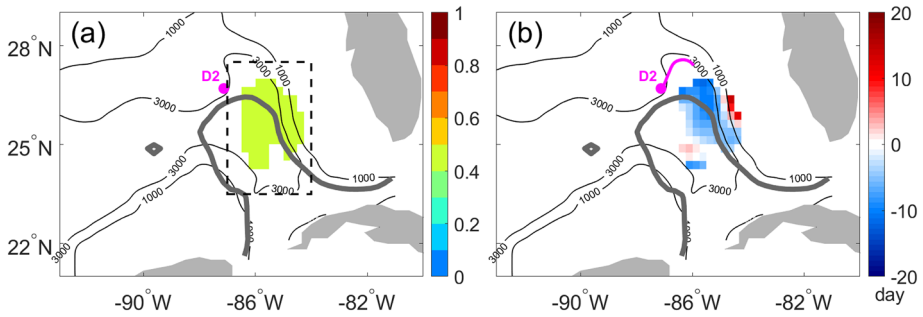

Figure 8. (a) Maximum lagged vector correlations (colored image) between the bottom velocities at mooring D2 and surface velocities at all SSH grid points and (b) associated time lags (colored image) corresponding to the maximum correlations. The correlations are normalized to range from 0 to 1, and only the correlations that are significant at the 95% confidence level are shown. Negative (positive) lag means surface fluctuations leading (lagging) near-bottom currents. The magenta line represents 10-day backward raypath for TRWs with a period of 60 days starting from D2. Thick gray contour denotes the mean SSH at 450 mm over the D2 observation period. Black contours are the 1,000 and 3,000-m isobaths. The black dashed rectangle in (a) represents the region where the CEOF analysis of surface zonal velocities is performed and shown in Figure 9.

The cointensification of the surface and bottom EKE and the nearly coherent vertical structure often exist under the unstable LC and LCEs. Away from the most unstable part of the LC, there is no clear link between the local surface and bottom EKE. As shown in Figures 6c and 6d, the surface and bottom EKE at mooring D2, which is north of the high-EKE region, does not show a clear relationship as at D4 (Figure 6b). Given that the correlation between the surface and bottom currents at the same location is small and not significant, the bottom currents at D2 likely have more energy originating from other areas.

To find surface fluctuations that could be responsible for the bottom motions at D2, maximum lagged vector correlations were calculated between the bottom current fluctuations at mooring D2 and surface current fluctuations at all surface grid points in the GoM. The maximum temporal lag was set as 100 days, which allowed us to track the surface current variability that was distant from the mooring site but potentially impacted the bottom ocean. Only maximum correlations significant at the 95% confidence level were kept, and the correlation map was further smoothed with a two-dimensional Gaussian filter with the half amplitude at 200 km, same as the spatial correlation scale of surface current data in the GoM (Pujol et al., 2016). If more than 50% of the points within a circle with a 100-km radius were significant, these points were kept for analyzing the dominant correlation pattern. Figure 8 shows the significant correlations and associated lags for mooring D2. It appears that the eastern side of the LC is critical not only for the local bottom currents but also for those away from the LC. The negative lags corresponding to the significant correlations indicate that the surface fluctuations in the eastern side of LC might be the energy source for the bottom currents in the northern LC. Note that the coupling process at D2 in the northern LC is different from that at D4 and L7 in the eastern LC where baroclinic instability is observed.

Bottom intensification at some times is found in Figure 7b, indicating possible existence of TRWs in the deep eastern GoM. Temporal lagged correlations of the bottom zonal velocity and EKE between D2 and D3 imply an upslope energy propagation and a downslope phase propagation, suggesting propagating TRWs in this region (Oey & Lee, 2002). It is plausible to partially explain the bottom currents with a remote energy source through the propagation of TRWs.

TRW ray tracing was used to trace the bottom EKE pathway in this study. The TRW dispersion relations and ray tracing equations are described in Appendix A1. At D2, the topographic slope parameter β_{topo} defined as $f|\nabla h|/h$ is equal to 7.2×10^{-11} m^{-1} s^{-1} and is much larger than the planetary beta of about 2×10^{-11} m^{-1} s^{-1}. As a result, the bottom topography effect dominates the planetary beta effect. Given a TRW period of 60 days, a constant N of 1×10^{-3} s^{-1}, and a starting point at D2, the wavenumber direction was estimated based on the simplified TRW dispersion relation (see Appendix A1). The magnitude of initial wavelength for the TRW ray tracing, 300 km, was adopted from the estimate in Hamilton (2009) at mooring L7 in the LC region.

With the initial wavenumber, the raypath was traced backward from D2 for 10 days and shown in Figure 8b. The 10-day raypath followed the topography tendency and pointed to the north of the eastern LC limb with significant correlations, indicating that at least part of the bottom EKE at D2 came from that downslope

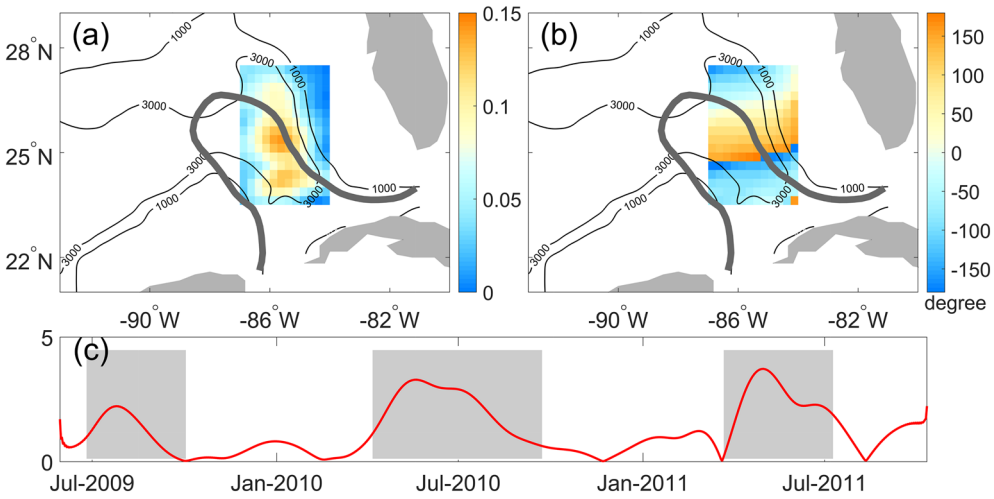

Figure 9. (a) CEOF Mode 1 spatial amplitudes (colored image) of the surface zonal velocities over the D4 observation period and (b) Mode 1 spatial phases (colored image). Thick gray contour denotes the mean SSH at 450 mm over the observation period of D4. Black contours are the 1,000- and 3,000-m isobaths. (c) Temporal amplitude of CEOF Mode 1 normalized by its standard deviation. Three periods with relatively large EKE same as those in Figure 6a are shaded in gray.

area. The associated temporal lags corresponding to the maximum correlations also show that the surface fluctuations over the eastern side of the LC mostly led the bottom currents at D2 by 10 days. Although the 10-day TRW ray does not reach the region with significant correlations, it points to that direction with a lag of few days, which can be caused by the approximation of environmental parameters. Based on the ray trace and maximum lagged correlations, the bottom currents at D2 were likely linked to surface fluctuations in the eastern LC limb.

To obtain the dominant mode of the surface variability over the critical region that was identified in Figure 8, complex empirical orthogonal function (CEOF) analysis (Horel, 1984), which was suitable for identifying propagating signals, was applied to the 30- to 90-day zonal velocities within that region. The CEOF analysis was performed to the complex time series formed by the original time series and their Hilbert transforms and yielded complex spatial and temporal mode patterns. The spatial amplitudes and phases of Mode 1, which explains 63% of the variance, show that the dominant surface mode is mesoscale fluctuations propagating southward along the eastern LC limb (Figures 9a and 9b). The large-amplitude area is consistent with the area of high EKE (Figure 6c). Both the spatial phases of the first mode CEOF (Figure 9b) and the temporal lags (Figure 8b) associated with the maximum lagged correlations suggest propagating signals. However, the southward propagating signals in the first mode CEOF are more apparent. One possible reason is that the southward propagating signals cannot account for all the correlations between the bottom and surface currents. The slowly propagating signals along the LC or zonally moving perturbations of the LC may also contribute to the coupling process. Figure 9c shows the Mode 1 temporal amplitude of the surface velocities. The temporal amplitude shows low-frequency variability associated with the long-period oscillation of the LC. When the LC was in unstable states with LCE detachments and separations, the amplitudes of surface and bottom EKE were amplified.

In sum, based on a subset of moorings in the LC region, the local coupling process through baroclinic instability and the remote coupling process through TRW excitation and propagation in the deep ocean were observed in the period band of 30 to 90 days. The surface fluctuations, especially those along the eastern LC limb, had stronger deep expressions on the short-period scale than on the long-period scale induced by the LC variation. A more vertically coherent structure was also observed during the unstable state of the LC. In addition, the coupling on the short-period scale was clearly modulated by the long-period LC variation.

3.2. The Central GoM

In the central northern GoM, large correlations are found in the shallow water rather than in the deep water around the Sigsbee Escarpment (Figure 5). EKE at two moorings, M4 and M2, are shown in Figure 10. At M4, which had a water depth of 1,333 m and was just north of the Sigsbee Escarpment, the bottom EKE

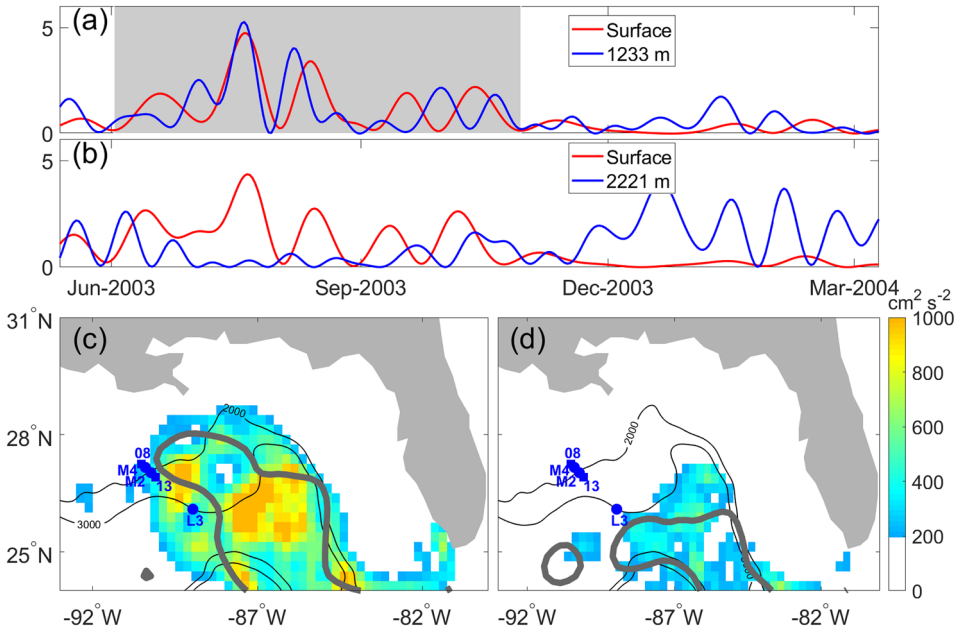

Figure 10. (a) EKE at the surface (red) and a bottom level (blue) at mooring M4 normalized by their standard deviations, 203.5 and 0.7 $cm^2\ s^{-2}$, respectively. The period with relatively large EKE is shaded in gray. (b) Surface (red) and bottom (blue) EKE at mooring M2 normalized by their standard deviations, 253.7 and 2.6 $cm^2\ s^{-2}$, respectively. (c) Mean surface EKE ($cm^2\ s^{-2}$, colored image) and mean SSH at 450 mm (thick gray contour) during the shaded period shown in (a). (d) Mean surface EKE and mean SSH at 450 mm at times with small EKE from November 2003 to March 2004 at M4. Mooring M2, M4, and L3 are represented by blue dots, and PIES Sites 08 and 13 are represented by blue filled squares. Black contours represent 2,000- and 3,000-m isobaths.

was enhanced when the surface EKE increased between June and October 2003. The enhanced EKE was related to an intrusion of the northern tip of the LC (Figure 10c), which was uncommon (Vukovich, 2007). After the LC shed a LCE and retracted southward, both the surface and bottom EKE stayed at a low level (Figure 10d). The mesoscale variability generated by the LC intrusion exerted the dominant impact in the water column above the Sigsbee Escarpment. In contrast, the bottom EKE at M2, which had a water depth of 2,321 m and was just south of the Sigsbee Escarpment, was not significantly affected by the increased surface EKE during the LC intrusion period (Figure 10b). After the LC retracted, the bottom EKE increased although the surface was quiet, indicating that the high bottom EKE likely originated from a remote source to the east (Hamilton, 2009).

No full-depth mooring was deployed around M2 and M4, but an array of PIES deployed in this region provided vertical profiles of temperature and salinity. Two PIES sites, named 08 and 13 (Figure 10d), were selected to examine the influence of surface mesoscale fluctuations on the deep ocean. Between June and November 2003, when the surface mesoscale variability in the northern edge of the LC passed, temperature anomalies in the period band of 30 to 90 days that were scaled by the temporal mean N^2 (squared Brunt-Väisälä frequency) were observed from the upper ocean to the bottom (Figure 11). It is noted that the temperature anomalies at PIES site 13 almost disappeared between 2,000 and 2,500 m and changed sign below 2,500 m (Figure 11b). The bottom currents at M2 were observed at 2,221 m where the temperature anomalies almost disappeared. The water depth difference between M2 and M4 could account for the different bottom response, because the surface-intensified vortices had more direct impacts on the bottom current in shallow water than that in deeper water when they crossed a steep slope.

In the deep water with a gentler topography than the Sigsbee Escarpment, high correlations were also observed at moorings such as L3. Figure 12 shows vertical profiles of the zonal velocities on the long-period scale (>90 days) and the short-period scale (30–90 days) at L3. The long-period velocities were strongly surface intensified and had a weak bottom expression. In contrast, the 30- to 90-day velocities showed a strong deep ocean response and a clear surface and bottom connection when the LC intruded northwestward. As the northwest part of the unstable LC moved to mooring L3 from May to September 2003, both bottom and surface currents were enhanced. Considering that the perturbations propagated in the direction of the

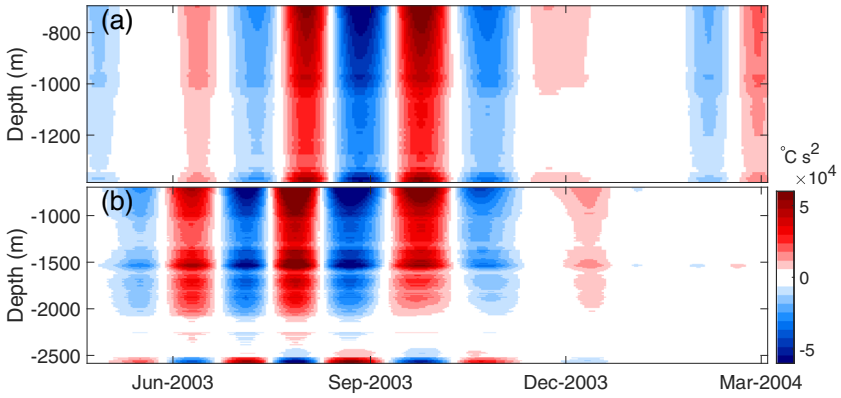

Figure 11. Depth-time section of temperature anomalies in the period band of 30 to 90 days and normalized by the mean squared Brunt-Väisälä frequency below the 700 m at the PIES Site 08 (a) and at the PIES Site 13 (b). The PIES sites are marked in Figure 10.

clockwise flowing LC, the zonal velocities in the bottom leading those at the surface by a few days were consistent with the signature of baroclinic instability. The bottom intensification was stronger than that in the LC region such as at L7 (Figure 7), which might be due to the steeper topography compared to the deep eastern GoM with its relatively flat bottom. After the LC retracted, the surface and bottom currents lost their direct connection.

To examine the impacts of the remote surface fluctuations, we also calculated the maximum lagged vector correlations between the bottom currents at mooring L3 and surface currents at all surface grid points in the GoM (Figure 13). The temporal lags associated with the maximum lagged correlations indicate that the northwestward and southwestward propagating signals are important for the significant correlations. The bottom intensification shown in Figure 12b suggests TRW propagation. Consequently, the TRW ray tracing was applied as in the LC region. The ratio of topographic beta to the planetary beta is about 6, which suggests that the bottom topography effect dominates the planetary beta effect. Given the starting point L3, a constant N of 1×10^{-3} s^{-1} and a wave period of 60 days, the wavenumber direction was calculated based on the simplified TRW dispersion relation (see Appendix A1). An initial wavelength of 203 km was adopted from the estimate in Hamilton (2009) based on the wavenumber analysis at L3, O1, O2, and Q2.

Starting from L3, the ray was traced backward for 12 days (Figure 13b). The ray reached the northeastern Mississippi Fan, where surface fluctuations led the bottom currents at L3 by about 12 days. The ray tracing indicates that besides the local coupling process, part of the bottom EKE at L3 could result from the TRW propagation from the northeastern Mississippi Fan. This observation agrees with Oey (2008), in which the fluctuations of the LC can induce deep ocean current variability both locally and remotely.

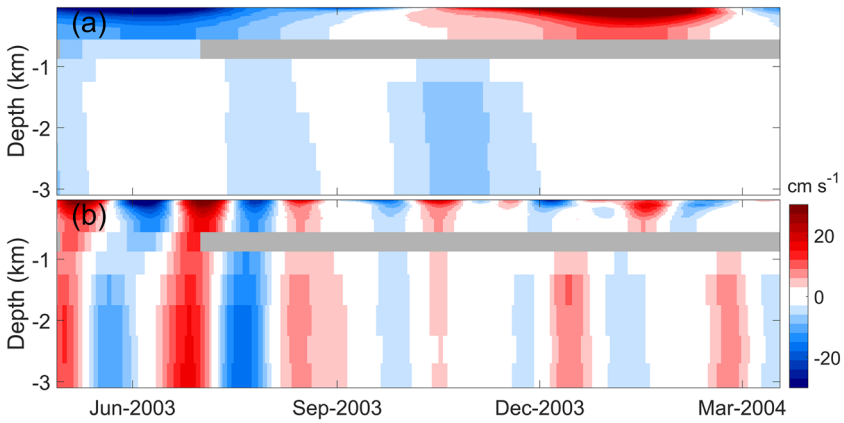

Figure 12. Depth-time section of the zonal velocities (cm s^{-1}) at mooring L3 (Figure 10c) for periods longer than 90 days (a) and for the period band of 30 to 90 days (b).

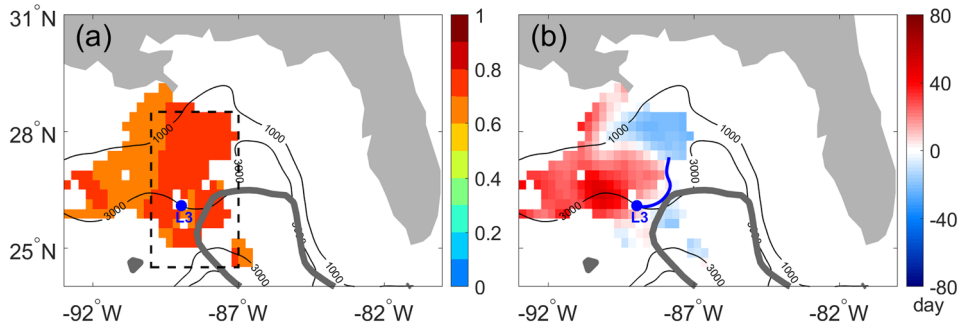

Figure 13. (a) Maximum lagged vector correlations (colored image) between the bottom velocities at mooring L3 and surface velocities at all SSH grid points and (b) associated time lags (colored image) corresponding to the maximum correlations. The correlations are normalized to range from 0 to 1, and only the correlations that are significant at the 95% confidence level are shown. Negative (positive) lag means surface fluctuations leading (lagging) near-bottom currents. The blue line represents 12-day backward raypath for TRWs with a period of 60 days starting from L3. Thick gray contour denotes the mean SSH at 450 mm over the observation period of mooring L3. Black contours are the 1,000- and 3,000-m isobaths. The black dashed rectangle in (a) represents the region where the surface zonal velocity CEOF (shown in Figure 14) is performed.

To further examine the dominant surface fluctuations that are responsible for the coupling, CEOF analysis was applied to the 30- to 90-day zonal velocities over the region marked in Figure 13a. The spatial amplitudes and phases of Mode 1, which explains 65% of the variance, show that the dominant surface mode is mesoscale fluctuations rotating clockwise around the northern LC that extends northwestward (Figures 14a and 14b). The large-amplitude region is consistent with the area of high EKE shown in Figure 10c. The temporal amplitude of surface fluctuations (Figure 14c) was modulated by the variability of the LC. When the unstable LC intruded northwestward during the first few months of the observation period, the amplitudes of surface currents and bottom currents were amplified (Figures 14c and 12b).

In sum, based on a subset of moorings in the central northern GoM, the surface fluctuations over the northern LC had significant effects on the near-bottom currents. In the deep water with gentle topography like the west side of the Mississippi Fan, the bottom currents were affected by both local and remote surface fluctuations. In the deep water with steep topography such as south of the Sigsbee Escarpment, the direct influence of the surface fluctuations was not as obvious as that in shallow water north of the Sigsbee Escarpment. Also, the coupling processes on the relatively short-period scale were modulated by the long-period LC variations.

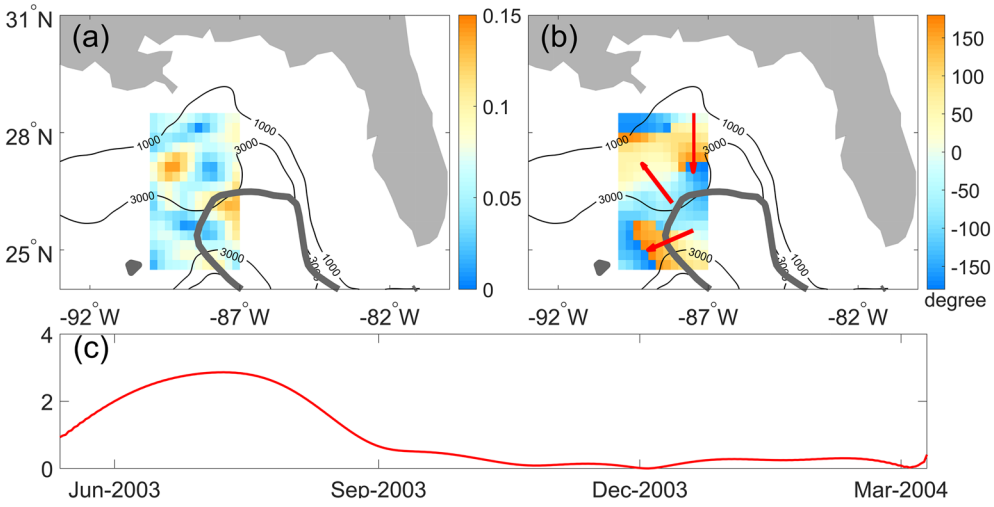

Figure 14. (a) CEOF Mode 1 spatial amplitudes (colored image) of the surface zonal velocities over the L3 observation period and (b) Mode 1 spatial phases (colored image). Thick gray contour denotes the mean SSH at 450 mm over the observation period. Black contours are the 1,000- and 3,000-m isobaths. Red arrows in (b) denote the wave propagation direction. (c) Temporal amplitude of the CEOF Mode 1 normalized by its standard deviation.

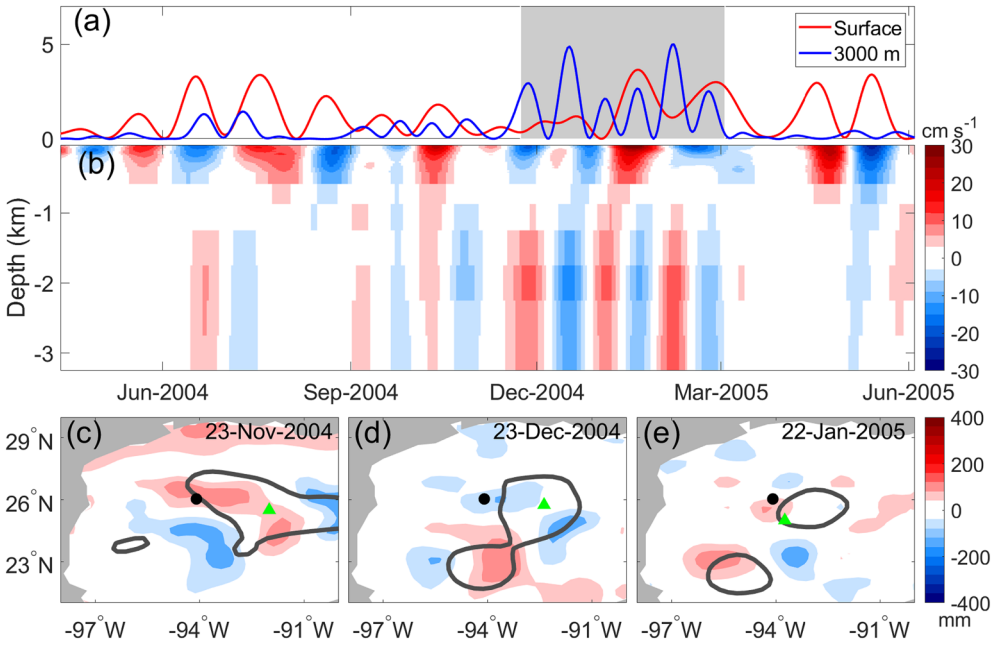

Figure 15. (a) EKE at the surface (red) and a bottom level (blue) at mooring V4 normalized by their standard deviations, 57.5 and 11.9 $cm^2\ s^{-2}$, respectively . The period with relatively large EKE is shaded in gray. (b) Depth-time section of the zonal velocities ($cm\ s^{-1}$) at mooring V4 in the period band of 30 to 90 days. (c–e) Snapshots of SSH anomalies in the period band of 30 to 90 days (colored maps) and the low-pass filtered SSH at 450 mm with periods longer than 90 days (thick gray contour) at 23 November 2004, 23 December 2004, and 22 January 2005, respectively. Mooring V4 is represented by the black dot. The green triangle represents the LCE center detected and tracked with the method proposed by Le Vu et al. (2018).

3.3. The Northwestern GoM

In a model study, Oey and Lee (2002) suggest that TRWs can originate from southwestward propagating LCEs and account for the lower-layer EKE in the northwestern GoM. The surface and bottom EKE at mooring V4 are shown in Figure 15a. Before October 2004, the local eddy activities dominated the surface variability with a relatively weak bottom response. After that time, one LCE that was shed from the LC traveled westward with a zonally elongated shape. Peripheral mesoscale fluctuations rotated round the LCE while traveling westward with the LCE. As the LCE arrived at V4 in November 2004, the bottom currents started to intensify but were not well correlated with the surface currents (Figure 15a). The LCE rotated clockwise and split into two parts (Figures 15c–15e) with the northern part moving slowly around V4. Although the bottom coherent currents were enhanced between November 2004 and March 2005 when the LCE arrived (Figure 15), a direct linkage between the surface and bottom currents was not as obvious as in the eastern GoM, implying that other remote processes such as westward propagating TRWs could be important. The currents in the northwestern GoM tended to have a more baroclinic structure (Figure 15b) than those in the LC region (Figure 7b). This might be related to the interactions of deep currents with the sea floor, and the topographic influence induced a more depth-dependent structure (Böning, 1989).

Since TRWs traveling from the east may contribute to the bottom current variability (Hamilton, 2009; Oey & Lee, 2002), maximum lagged correlations and TRW ray tracing were explored. Maximum lagged vector correlations between the bottom currents at mooring V4 and the surface currents at all surface grid points in the GoM were calculated. At the 95% confidence level, the correlations did not yield a significant correlation pattern. However, maximum lagged correlations for EKE yielded a significant spatial correlation pattern (Figure 16). The near-bottom currents in the northwestern GoM appeared to have a connection with the remote surface variability originating from the west side of the LC. The west side of the LC has been shown to be a birth place of eddies and TRWs, which are associated with the movements of the LC and eddy sheddings (Oey, 2008). For example, one LCE was shed from the LC in August 2004 and could provide KE for the bottom currents in the northwestern GoM. The temporal lags (Figure 16b) indicate that the surface fluctuations in the eastern and central GoM could lead the bottom currents in the northwestern GoM before they got close

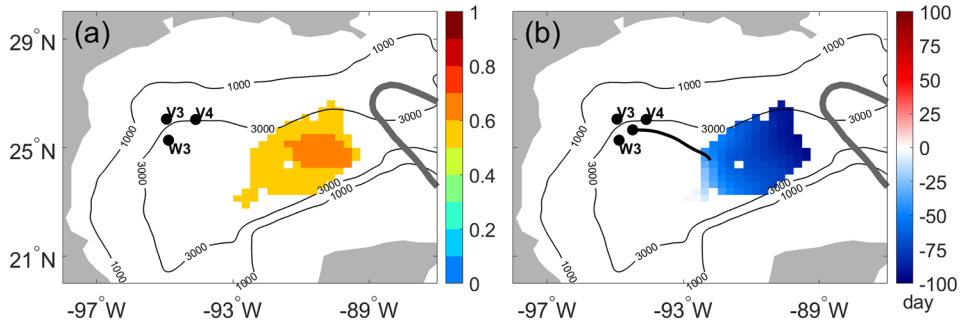

Figure 16. (a) Maximum lagged correlations (colored image) between the bottom EKE at mooring V4 and the surface EKE at all SSH grid points and (b) associated time lags (colored image) corresponding to the maximum correlations. Only the correlations that are significant at the 95% confidence level are shown. Negative (positive) lag means surface fluctuations leading (lagging) near-bottom currents. Black dots represent mooring W3, V3, and V4 and one starting point for the TRWs ray tracing. The black line represents the 25-day backward raypath for TRWs with a period of 60 days from the point between W3 and V4. Thick gray contour denotes the mean SSH at 450 mm over the observation period. Black contours are the 1,000- and 3,000-m isobaths.

to the mooring site. In the TRW ray tracing, the initial wavelength estimated in Hamilton (2009) based on the observations at V3, V4, and W3 was used here. Given one selected starting point between W3 and V4 (Figure 16b), a constant N of 1×10^{-3} s^{-1}, and a wave period of 60 days, the wavenumber vector direction was again estimated from the simplified dispersion relation (see Appendix A1). The ray was traced backward for 25 days, reaching the western edge of the significant correlation patch. At the end of the TRW ray, the surface fluctuations led the bottom currents at V4 by about 30 days, which was close to the transit time of the TRW energy along the 25-day track. The ray tracing indicates that TRWs in the northwestern GoM could be traced back to the surface fluctuations traveling westward from the west of the LC.

The above analyses for mooring V4 imply that the LCE might have a local impact on the bottom currents when it arrived at the northwestern GoM, but the local impact was relatively weak compared to that in the eastern GoM. More importantly, the surface fluctuations traveling westward from the west of the LC could excite northwestward propagating TRWs. In addition, the locally forced fluctuations and the remnant of LCEs in the southwestern GoM also might play a role in driving the bottom current variability, which was reported by Donohue et al. (2008). One previous case study by Donohue et al. (2008) suggests that the coupling involves the lower-layer compression or stretching by the upper-layer eddies.

4. Conclusions and Discussions

Deep ocean currents are important in modulating and generating internal waves, ocean mixing and in the dispersal of biogeochemical properties (e.g., Adams et al., 2011; Brearley et al., 2013; Cardona et al., 2016; Díaz-Asencio et al., 2019; Gardner et al., 2017; Liang, 2014; Liang & Thurnherr, 2012; Nikurashin & Ferrari, 2010a, 2010b). They have been shown to be able to connect to upper-ocean fluctuations such as mesoscale eddies in different oceans (e.g., Liang & Thurnherr, 2011; Tenreiro et al., 2018; Zhang et al., 2013, 2016). Since the bottom currents are rarely observed and reported, it would be useful if we knew more about the connections between the surface and bottom currents.

In this study, a combination of surface geostrophic currents derived from SSH observations and near-bottom currents from historical mooring arrays was used to examine the coupling of the surface and near-bottom currents in the GoM in the period band of 30 to 90 days. Their coupling involves both local processes such as baroclinic instability and remote processes through TRW propagation. The dominant mode of upper-ocean fluctuations responsible for the variability of near-bottom currents is mesoscale variability that is generated along the LC and the westward propagating LCEs. The short-period fluctuations (30–90 days) have stronger bottom expressions and a more vertically coherent structure than the long-period (>90 days) oscillations related to large-scale LC intrusions.

Although the statistical results of coupling should be interpreted with caution owing to the short length of bottom current records, the LC region in the eastern GoM facilitates more significant couplings than other regions. Moreover, the surface fluctuations that are responsible for the coupling vary geographically. In the LC region, the surface fluctuations along the eastern LC are important in causing bottom fluctuations

Table 3
Dominant Processes for Surface and Bottom Coupling in Three Regions of the GoM

Mooring location	Responsible surface fluctuations	Dominant processes
LC region	Fluctuations along the eastern LC	Local baroclinic instability; remote TRW propagation
Central GoM	Fluctuations along the northern LC	Local baroclinic instability; remote TRW propagation
Northwestern GoM	Fluctuations associated with LCEs shed from the eastern GoM	Remote TRW propagation

through baroclinic instability under the LC and through TRW propagation north of the LC. Our findings are generally consistent with the earlier case studies (e.g., Donohue et al., 2016; Hamilton et al., 2014; Hamilton, Lugo-Fernández, et al., 2016). In the central deep GoM, the bottom currents are affected by the mesoscale variability of the northern LC through both local baroclinic instability and remote TRW propagation from the eastern Mississippi Fan. Also, the remote surface variability associated with LCEs traveling from the west side of the LC can excite northwestward propagating TRWs, leading to bottom current fluctuations in the northwestern GoM. The local impact of the LCEs in the western GoM on the bottom currents is relatively weak compared to that in the eastern GoM. The most important coupling processes in the three regions of the GoM are summarized in Table 3.

The coupling processes presented in this study are commonly seen in the ocean current observations and have been reported in previous studies. Nevertheless, the statistical analysis such as correlation used in this study may be dominated by a few events in the yearlong time series and cannot lead to a determinate conclusion on the coupling pattern. To examine that, we obtained the HYCOM reanalysis and calculated the maximum lagged vector correlations between the bottom currents at each mooring point and surface currents at all surface grid points in the GoM between January 2000 and December 2010. The maximum lagged vector correlations were averaged at the mooring sites where a significant spatial pattern existed. Similar to the pattern found in the observations (Figure 17a), the locations with significant correlations are mostly found in the LC region, although the mean correlations are smaller, ranging from 0.2 to 0.4 (Figure 17b). The similar correlation patterns inferred from observations and HYCOM reanalysis imply that the surface and bottom coupling is quite robust in the LC region.

In this study, we focus mainly on describing features of the coupling of the surface and bottom current fluctuations in the GoM. In spite of the limitations of sparse near-bottom current observations, the surface and bottom coupling features in different parts of the GoM are obtained, providing a reference of where significant coupling is likely to be detected and what physical processes might be the dominant causes. However, the coupling mechanisms are more complicated than merely involving baroclinic instability and TRW propagation. For example, potential vorticity anomalies in the deep ocean induced by the upper-ocean perturbations can contribute to the coupling process as well (e.g., Donohue et al., 2008; Hamilton, 2009; Hamilton et al., 2019; Tenreiro et al., 2018), which is not analyzed in this study. Baroclinic Kelvin waves are

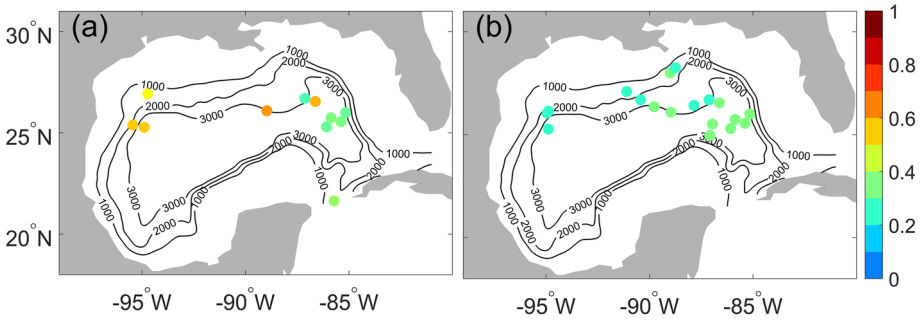

Figure 17. Mean correlation values calculated by averaging the spatial maximum lagged vector correlations between the near-bottom currents at each mooring and surface currents at all grid points from (a) observations and (b) HYCOM reanalysis between 2000 and 2010. The maximum lagged vector correlations are normalized to range from 0 to 1, and only those significant at the 95% confidence level are used. The moorings without significant correlations are not shown. Black contours are 1,000-, 2,000-, and 3,000-m isobaths.

one of the other physical processes that might be related to the deep ocean fluctuations (e.g., Sheinbaum et al., 2010). All these will be explored in future studies.

Appendix A: TRW Ray Tracing

The full TRW dispersion relations are given by the following equations (e.g., Hamilton, 2009; Oey & Lee, 2002):

$$\lambda^2 = \left(k^2 + l^2 + \frac{\beta k}{\omega}\right)\left(\frac{N}{f}\right)^2 \tag{A1}$$

$$\lambda tanh(\lambda h) = \frac{N^2}{\omega f}(kh_y - lh_x) \tag{A2}$$

where k and l are the zonal and meridional wavenumber, respectively, f is the Coriolis parameter, β is the meridional gradient of the Coriolis parameter, ω is the wave frequency, N is the Brunt-Väisälä frequency in the deep layer, h is the water depth, and h_x and h_y are the zonal and meridional gradient of water depth, respectively.

The governing equations of wave path and its wavenumber are as follows (LeBlond & Mysak, 1978):

$$\frac{\mathrm{d}\vec{x}}{\mathrm{d}t} = \frac{\partial\omega}{\partial\vec{k}} = \vec{c}_g \tag{A3}$$

$$\frac{\mathrm{d}\vec{k}}{\mathrm{d}t} = \sum -\frac{\partial\omega}{\partial\gamma_i}\nabla\gamma_i \tag{A4}$$

where $\frac{\mathrm{d}}{\mathrm{d}t} = \frac{\partial}{\partial t} + \vec{c}_g \cdot \nabla$ is the derivative following the wave group, $\vec{x}$ is the raypath, $\vec{c}_g$ is the group velocity, and γ_i are the environmental parameters with larger scale than the wavelength, including h, h_x, and h_y. N is assumed constant and equal to 1×10^{-3} s^{-1}. Raypaths are obtained by integrating the governing equations of wave path and its wavenumber with the fourth-order Runge-Kutta method, which has been used in Hamilton (2009), Kolodziejczyk et al. (2011), and Oey and Lee (2002).

If the bottom topography effect dominates the planetary beta effect, the planetary beta term can be dropped in the TRW dispersion relation. For $\lambda h \geq 1$, the TRW dispersion relation can be approximated by $\omega = N|\nabla h|sin(\theta)$, where θ is the clockwise angle that the wavenumber vector makes with the topography gradient (Oey & Lee, 2002). The wavenumber vector direction can be estimated if ω, N, and $|\nabla h|$ are given.

Data Availability Statement

SSH data were produced and provided by CMEMS. The SSH and surface current fields used in this study are available at https://dx.doi.org/10.7266/n7-ya5j-0t90 (Zhu, 2020b). Historical mooring data in the GoM were collected from GRIIDC and NOAA/NCEI. The subsurface current data from the moorings are freely accessible at https://dx.doi.org/10.7266/n7-7g3d-9q79 (Zhu, 2020c). The HYCOM reanalysis data provided by HYCOM Consortium are available at https://dx.doi.org/10.7266/n7-2zxg-x010 (Zhu, 2020a). Temperature profiles from the PIES observations are accessible online (https://data.noaa.gov/onestop/collections/details/AWbwm-H7HtVRBOAZkBYZ). The bathymetry data were downloaded from GRIIDC at https://dx.doi.org/10.7266/N7X63JZ5 (Panagiotis, 2014).

Acknowledgments
We thank three anonymous reviewers for their constructive comments and suggestions. We also thank Drs. Jennifer Bonin and Pablo Huq for proofreading the manuscript. The work was supported by the Gulf of Mexico Research Initiative through Grant G-231804 and the National Aeronautics and Space Administration through Grant 80NSSC20K0757.

References

Adams, D. K., McGillicuddy, D. J., Zamudio, L., Thurnherr, A. M., Liang, X., Rouxel, O., et al. (2011). Surface-generated mesoscale eddies transport deep-sea products from hydrothermal vents. *Science*, *332*(6029), 580–583. https://doi.org/10.1126/science.1201066

Alvera-Azcárate, A., Barth, A., & Weisberg, R. H. (2009). The surface circulation of the caribbean sea and the Gulf of Mexico as inferred from satellite altimetry. *Journal of Physical Oceanography*, *39*(3), 640–657. https://doi.org/10.1175/2008JPO3765.1

Böning, C. W. (1989). Influences of a rough bottom topography on flow kinematics in an eddy-resolving circulation model. *Journal of Physical Oceanography*, *19*(1), 77–97. https://doi.org/10.1175/1520-0485(1989)019<0077:IOARBT>2.0.CO;2

Brearley, J. A., Sheen, K. L., Naveira Garabato, A. C., Smeed, D. A., & Waterman, S. (2013). Eddy-induced modulation of turbulent dissipation over rough topography in the Southern Ocean. *Journal of Physical Oceanography*, *43*(11), 2288–2308. https://doi.org/10.1175/JPO-D-12-0222.1

Cardona, Y., & Bracco, A. (2016). Predictability of mesoscale circulation throughout the water column in the Gulf of Mexico. *Deep Sea Research Part II: Topical Studies in Oceanography*, *129*, 332–349. The Gulf of Mexico Ecosystem - before, during and after the Macondo Blowout. https://doi.org/10.1016/j.dsr2.2014.01.008

Cardona, Y., Ruiz-Ramos, D. V., Baums, I. B., & Bracco, A. (2016). Potential connectivity of coldwater black coral communities in the northern Gulf of Mexico. *PLOS ONE*, *11*(5), 1–25. https://doi.org/10.1371/journal.pone.0156257

Chang, Y.-L., & Oey, L.-Y. (2011). Loop current cycle: Coupled response of the loop current with deep flows. *Journal of Physical Oceanography*, *41*(3), 458–471. https://doi.org/10.1175/2010JPO4479.1

Chérubin, L. M., Morel, Y., & Chassignet, E. P. (2006). Loop current ring shedding: The formation of cyclones and the effect of topography. *Journal of Physical Oceanography*, *36*(4), 569–591. https://doi.org/10.1175/JPO2871.1

Chérubin, L. M., Sturges, W., & Chassignet, E. P. (2005). Deep flow variability in the vicinity of the Yucatan straits from a high-resolution numerical simulation. *Journal of Geophysical Research*, *110*, C04009. https://doi.org/10.1029/2004JC002280

Crosby, D. S., Breaker, L. C., & Gemmill, W. H. (1993). A proposed definition for vector correlation in geophysics: Theory and application. *Journal of Atmospheric and Oceanic Technology*, *10*(3), 355–367. https://doi.org/10.1175/1520-0426(1993)010<0355:APDFVC>2.0.CO;2

Cummings, J. A. (2005). Operational multivariate ocean data assimilation. *Quarterly Journal of the Royal Meteorological Society*, *131*(613), 3583–3604. https://doi.org/10.1256/qj.05.105

Cushman-Roisin, B., Tang, B., & Chassignet, E. P. (1990). Westward motion of mesoscale eddies. *Journal of Physical Oceanography*, *20*(5), 758–768. https://doi.org/10.1175/1520-0485(1990)020<0758:WMOME>2.0.CO;2

DiMarco, S. (2014). Ocean current, temperature and salinity time series, g04 moorings, deepwater horizon oil spill region, july 2012 to july 2013. Distributed by: Gulf of Mexico Research Initiative Information and Data Cooperative (GRIIDC), Harte Research Institute, Texas A&M UniversityCorpus Christi https://doi.org/10.7266/N7930R44

DiMarco, S. (2016). Ocean current, temperature and salinity time series, g06 moorings, deepwater horizon oil spill region, July 2013 to July 2014. Distributed by: Gulf of Mexico Research Initiative Information and Data Cooperative (GRIIDC), Harte Research Institute, Texas A&M UniversityCorpus Christi https://doi.org/10.7266/N7G15XWT

DiMarco, S., Nowlin, W. D. Jr., & Reid, R. O. (2005). A statistical description of the velocity fields from upper ocean drifters in the Gulf of Mexico, *Circulation in the Gulf of Mexico: Observations and models* (pp. 101–110): American Geophysical Union (AGU).

Díaz-Asencio, M., Bartrina, V. F., & Herguera, J. C. (2019). Sediment accumulation patterns on the slopes and abyssal plain of the southern Gulf of Mexico. *Deep Sea Research Part I: Oceanographic Research Papers*, *146*, 11–23. https://doi.org/10.1016/j.dsr.2019.01.003

Donohue, K., Hamilton, P., Leaman, K., Leben, R., Prater, M., Watts, D. R., & Waddell, E. (2006). Exploratory study of deepwater currents in the Gulf of Mexico, volume II 2: (Tech. Rep. No. OCS Study MMS 2006-074). New Orleans, LA: U.S. Dept. of the Interior, Minerals Management Service, Gulf of Mexico OCS Region.

Donohue, K., Hamilton, P., Leben, R., Watts, R., & Waddell, E. (2008). Survey of deepwater currents in the northwestern Gulf of Mexico, volume II 2: (Tech. Rep. No. OCS Study MMS 2008-031). New Orleans, LA: U.S. Dept. of the Interior, Minerals Management Service, Gulf of Mexico OCS Region.

Donohue, K. A., Watts, D. R., Hamilton, P., Leben, R., & Kennelly, M. (2016). Loop current eddy formation and baroclinic instability. *Dynamics of Atmospheres and Oceans*, *76*, 195–216. The Loop Current Dynamics Experiment https://doi.org/10.1016/j.dynatmoce.2016.01.004

Elliott, B. A. (1982). Anticyclonic rings in the Gulf of Mexico. *Journal of Physical Oceanography*, *12*(11), 1292–1309. https://doi.org/10.1175/1520-0485(1982)012<1292:ARITGO>2.0.CO;2

Frolov, S. A., Sutyrin, G. G., Rowe, G. D., & Rothstein, L. M. (2004). Loop current eddy interaction with the western boundary in the Gulf of Mexico. *Journal of Physical Oceanography*, *34*(10), 2223–2237. https://doi.org/10.1175/1520-0485(2004)034<2223:LCEIWT>2.0.CO;2

Furey, H., Bower, A., Perez-Brunius, P., Hamilton, P., & Leben, R. (2018). Deep eddies in the Gulf of Mexico observed with floats. *Journal of Physical Oceanography*, *48*(11), 2703–2719. https://doi.org/10.1175/JPO-D-17-0245.1

Gardner, W. D., Tucholke, B. E., Richardson, M. J., & Biscaye, P. E. (2017). Benthic storms, nepheloid layers, and linkage with upper ocean dynamics in the western North Atlantic. *Marine Geology*, *385*, 304–327. https://doi.org/10.1016/j.margeo.2016.12.012

Hamilton, P. (1990). Deep currents in the Gulf of Mexico. *Journal of Physical Oceanography*, *20*(7), 1087–1104. https://doi.org/10.1175/1520-0485(1990)020<1087:DCITGO>2.0.CO;2

Hamilton, P. (2007). Deep-current variability near the Sigsbee Escarpment in the Gulf of Mexico. *Journal of Physical Oceanography*, *37*(3), 708–726. https://doi.org/10.1175/JPO2998.1

Hamilton, P. (2009). Topographic Rossby waves in the Gulf of Mexico. *Progress in Oceanography*, *82*(1), 1–31. https://doi.org/10.1016/j.pocean.2009.04.019

Hamilton, P., Berger, T. J., Singer, J. J., Waddell, E., Churchill, J. H., Leben, R. R., et al. (2000). Desoto canyon eddy intrusion study, final report, volume II 2: (Tech. Rep. No. OCS Study MMS 2000-080). New Orleans, LA: U.S. Dept. of the Interior, Minerals Management Service, Gulf of Mexico OCS Region.

Hamilton, P., Bower, A., Furey, H., Leben, R. R., & Pérez-Brunius, P. (2016). Deep circulation in the Gulf of Mexico: A lagrangian study (Tech. Rep. No. OCS Study BOEM 2016-081). New Orleans, LA: U.S. Dept. of the Interior, Bureau of Ocean Energy Management, Gulf of Mexico OCS Region.

Hamilton, P., Bower, A., Furey, H., Leben, R., & Pérez-Brunius, P. (2019). The loop current: Observations of deep eddies and topographic waves. *Journal of Physical Oceanography*, *49*(6), 1463–1483. https://doi.org/10.1175/JPO-D-18-0213.1

Hamilton, P., Donohue, K., Hall, C., Leben, R. R., Quian, H., Sheinbaum, J., & Watts, D. R. (2014). Observations and dynamics of the loop current (Tech. Rep. No. OCS Study BOEM 2015-006). New Orleans, LA: U.S. Dept. of the Interior, Bureau of Ocean Energy Management, Gulf of Mexico OCS Region.

Hamilton, P., Lugo-Fernández, A., & Sheinbaum, J. (2016). A loop current experiment: Field and remote measurements. *Dynamics of Atmospheres and Oceans*, *76*, 156–173. The Loop Current Dynamics Experiment https://doi.org/10.1016/j.dynatmoce.2016.01.005

Hamilton, P., Singer, J. J., Waddell, E., & Donohue, K. (2003). Deepwater observations in the northern Gulf of Mexico from in-situ current meters and pies, technical report, volume II 2: (Tech. Rep. No. OCS Study MMS 2003-049). New Orleans, LA: U.S. Dept. of the Interior, Minerals Management Service, Gulf of Mexico OCS Region.

Horel, J. D. (1984). Complex principal component analysis: Theory and examples. *Journal of Climate and Applied Meteorology*, *23*(12), 1660–1673. https://doi.org/10.1175/1520-0450(1984)023<1660:CPCATA>2.0.CO;2

Hurlburt, H. E., & Thompson, J. D. (1980). A numerical study of loop current intrusions and eddy shedding. *Journal of Physical Oceanography*, *10*(10), 1611–1651. https://doi.org/10.1175/1520-0485(1980)010<1611:ANSOLC>2.0.CO;2

Inoue, M., Welsh, S. E., Rouse, L. J. Jr., & Weeks, E. (2008). Deepwater currents in the eastern Gulf of Mexico: Observations at 25.5 °N and 87°W (Tech. Rep. No. OCS Study MMS 2008-001). New Orleans, LA: U.S. Dept. of the Interior, Minerals Management Service, Gulf of Mexico OCS Region.

Kolodziejczyk, N., Ochoa, J., Candela, J., & Sheinbaum, J. (2011). Deep currents in the Bay of Campeche. *Journal of Physical Oceanography*, *41*(10), 1902–1920. https://doi.org/10.1175/2011JPO4526.1

Kolodziejczyk, N., Ochoa, J., Candela, J., & Sheinbaum, J. (2012). Observations of intermittent deep currents and eddies in the Gulf of Mexico. *Journal of Geophysical Research*, *117*, C09014. https://doi.org/10.1029/2012JC007890

LaCasce, J. H. (1998). A geostrophic vortex over a slope. *Journal of Physical Oceanography*, *28*(12), 2362–2381. https://doi.org/10.1175/1520-0485(1998)028<2362:AGVOAS>2.0.CO;2

Le Vu, B., Stegner, A., & Arsouze, T. (2018). Angular momentum eddy detection and tracking algorithm (AMEDA) and its application to coastal eddy formation. *Journal of Atmospheric and Oceanic Technology*, *35*(4), 739–762. https://doi.org/10.1175/JTECH-D-17-0010.1

LeBlond, P. H., & Mysak, L. A. (1978). *Waves in the ocean*. New York: Elsevier Scientific Publishing Company.

Leben, R. R. (2005). Altimeter-derived loop current metrics, *Circulation in the Gulf of Mexico: Observations and models* (pp. 181–201). Washington, DC: American Geophysical Union (AGU). https://doi.org/10.1029/161GM15

Lee, H.-C., & Mellor, G. L. (2003). Numerical simulation of the gulf stream system: The loop current and the deep circulation. *Journal of Geophysical Research*, *108*(C2), 3043. https://doi.org/10.1029/2001JC001074

Liang, X. (2014). Semidiurnal tidal currents in the deep ocean near the East Pacific rise between 9° and 10°N. *Journal of Geophysical Research: Oceans*, *119*, 4264–4277. https://doi.org/10.1002/2013JC009522

Liang, X., & Thurnherr, A. M. (2011). Subinertial variability in the deep ocean near the East Pacific rise between 9° and 10°N. *Geophysical Research Letters*, *38*, L06606. https://doi.org/10.1029/2011GL046675

Liang, X., & Thurnherr, A. M. (2012). Eddy-modulated internal waves and mixing on a midocean ridge. *Journal of Physical Oceanography*, *42*(7), 1242–1248. https://doi.org/10.1175/JPO-D-11-0126.1

Liu, Y., Weisberg, R. H., Vignudelli, S., & Mitchum, G. T. (2016). Patterns of the loop current system and regions of sea surface height variability in the eastern Gulf of Mexico revealed by the self-organizing maps. *Journal of Geophysical Research: Oceans*, *121*, 2347–2366. https://doi.org/10.1002/2015JC011493

McKone, K., Walker, N. D., & Weeks, E. (2007). Full-water column currents near the Sigsbee Escarpment (91-92°W. longitude) and relationships with the loop current and associated warm and cold-core eddies (Tech. Rep. No. OCS Study MMS 2007-056). New Orleans, LA: U.S. Dept. of the Interior, Minerals Management Service, Gulf of Mexico OCS Region.

Morey, S. L., Gopalakrishnan, G., Sanz, E. P., Azevedo Correia De Souza, J. M., Donohue, K., Prez-Brunius, P., et al. (2020). Assessment of numerical simulations of deep circulation and variability in the Gulf of Mexico using recent observations. *Journal of Physical Oceanography*, *50*(4), 1045–1064. https://doi.org/10.1175/JPO-D-19-0137.1

Nikurashin, M., & Ferrari, R. (2010a). Radiation and dissipation of internal waves generated by geostrophic motions impinging on small-scale topography: Theory. *Journal of Physical Oceanography*, *40*(5), 1055–1074.

Nikurashin, M., & Ferrari, R. (2010b). Radiation and dissipation of internal waves generated by geostrophic motions impinging on small-scale topography: Application to the Southern Ocean. *Journal of Physical Oceanography*, *40*(9), 2025–2042. https://doi.org/10.1175/2009JPO4199.1

Oey, L.-Y. (1996). Simulation of mesoscale variability in the Gulf of Mexico: Sensitivity studies, comparison with observations, and trapped wave propagation. *Journal of Physical Oceanography*, *26*(2), 145–175. https://doi.org/10.1175/1520-0485(1996)026<0145:SOMVIT>2.0.CO;2

Oey, L.-Y. (2008). Loop current and deep eddies. *Journal of Physical Oceanography*, *38*(7), 1426–1449. https://doi.org/10.1175/2007JPO3818.1

Oey, L.-Y., Chang, Y.-L., Sun, Z.-B., & Lin, X.-H. (2009). Topocaustics. *Ocean Modelling*, *29*(4), 277–286. https://doi.org/10.1016/j.ocemod.2009.05.006

Oey, L.-Y., & Lee, H.-C. (2002). Deep eddy energy and topographic Rossby waves in the Gulf of Mexico. *Journal of Physical Oceanography*, *32*(12), 3499–3527. https://doi.org/10.1175/1520-0485(2002)032<3499:DEEATR>2.0.CO;2

Panagiotis, V. (2014). Gulf of Mexico high-resolution (0.01° × 0.01°) bathymetric grid - version 2.0, February 2013. Distributed by: Gulf of Mexico Research Initiative Information and Data Cooperative (GRIIDC), Harte Research Institute, Texas A&M UniversityCorpus Christi https://doi.org/10.7266/N7X63JZ5

Pérez-Brunius, P., Furey, H., Bower, A., Hamilton, P., Candela, J., García-Carrillo, P., & Leben, R. (2018). Dominant circulation patterns of the deep Gulf of Mexico. *Journal of Physical Oceanography*, *48*(3), 511–529. https://doi.org/10.1175/JPO-D-17-0140.1

Pujol, M.-I., Faugère, Y., Taburet, G., Dupuy, S., Pelloquin, C., Ablain, M., & Picot, N. (2016). Duacs dt2014: The new multi-mission altimeter data set reprocessed over 20years. *Ocean Science*, *12*(5), 1067–1090. https://doi.org/10.5194/os-12-1067-2016

Romanou, A., Chassignet, E. P., & Sturges, W. (2004). Gulf of Mexico circulation within a high-resolution numerical simulation of the North Atlantic Ocean. *Journal of Geophysical Research*, *109*, C01003. https://doi.org/10.1029/2003JC001770

Schmitz, W. J. Jr. (2005). Cyclones and westward propagation in the shedding of anticyclonic rings from the loop current, *Circulation in the Gulf of Mexico: Observations and models* (pp. 241–261). Washington, DC: American Geophysical Union (AGU). https://doi.org/10.1029/161GM18

Sheinbaum, J., Ochoa, J., Candela, J., & Badan, A. (2010). Full-water column current observations in the western Gulf of Mexico: Final report (Tech. Rep. No. OCS Study BOEMRE 2010-044). New Orleans, LA: U.S. Dept. of the Interior, Bureau of Ocean Energy Management, Regulation, and Enforcement, Gulf of Mexico OCS Region.

Sturges, W., Evans, J. C., Welsh, S., & Holland, W. (1993). Separation of warm-core rings in the Gulf of Mexico. *Journal of Physical Oceanography*, *23*(2), 250–268. https://doi.org/10.1175/1520-0485(1993)023<0250:SOWCRI>2.0.CO;2

Sturges, W., & Leben, R. (2000). Frequency of ring separations from the loop current in the Gulf of Mexico: A revised estimate. *Journal of Physical Oceanography*, *30*(7), 1814–1819. https://doi.org/10.1175/1520-0485(2000)030<1814:FORSFT>2.0.CO;2

Sun, Z., Zhang, Z., Qiu, B., Zhang, X., Zhou, C., Huang, X., et al. (2020). Three-dimensional structure and interannual variability of the Kuroshio Loop Current in the northeastern South China Sea. *Journal of Physical Oceanography*, *50*, 2437–2455. https://doi.org/10.1175/JPO-D-20-0058.1

Tenreiro, M., Candela, J., Sanz, E. P., Sheinbaum, J., & Ochoa, J. (2018). Near-surface and deep circulation coupling in the western Gulf of Mexico. *Journal of Physical Oceanography*, *48*(1), 145–161. https://doi.org/10.1175/JPO-D-17-0018.1

Thomson, R. E., & Emery, W. J. (2014). *Data analysis methods in physical oceanography*. Amsterdam: Elsevier Science.

Vukovich, F. M. (1995). An updated evaluation of the loop current's eddy-shedding frequency. *Journal of Geophysical Research*, *100*(C5), 8655–8659. https://doi.org/10.1029/95JC00141

Vukovich, F. M. (2007). Climatology of ocean features in the Gulf of Mexico using satellite remote sensing data. *Journal of Physical Oceanography*, *37*(3), 689–707. https://doi.org/10.1175/JPO2989.1

Weisberg, R. H., & Liu, Y. (2017). On the loop current penetration into the Gulf of Mexico. *Journal of Geophysical Research: Oceans*, *122*, 9679–9694. https://doi.org/10.1002/2017JC013330

Welsh, S. E., & Inoue, M. (2000). Loop current rings and the deep circulation in the Gulf of Mexico. *Journal of Geophysical Research*, *105*(C7), 16,951–16,959. https://doi.org/10.1029/2000JC900054

Welsh, S. E., Inoue, M., Rouse, L. J., & Weeks, E. (2009). Observation of the deepwater manifestation of the loop current and loop current rings in the eastern Gulf of Mexico (Tech. Rep. No. OCS Study MMS 2009-050). New Orleans, LA: U.S. Dept. of the Interior, Minerals Management Service, Gulf of Mexico OCS Region.

Xu, F.-H., Chang, Y.-L., Oey, L.-Y., & Hamilton, P. (2013). Loop current growth and eddy shedding using models and observations: Analyses of the july 2011 eddy-shedding event. *Journal of Physical Oceanography*, *43*(5), 1015–1027. https://doi.org/10.1175/JPO-D-12-0138.1

Zhang, Z., Tian, J., Qiu, B., Zhao, W., Chang, P., Wu, D., & Wan, X. (2016). Observed 3D structure, generation, and dissipation of oceanic mesoscale eddies in the South China Sea. *Scientific Reports*, *6*, 24349. https://doi.org/10.1038/srep24349

Zhang, Z., Zhao, W., Tian, J., & Liang, X. (2013). A mesoscale eddy pair southwest of Taiwan and its influence on deep circulation. *Journal of Geophysical Research: Oceans*, *118*, 6479–6494. https://doi.org/10.1002/2013JC008994

Zhu, Y. (2020a). Daily average velocity fields derived from HYCOM + NCODA Gulf of Mexico reanalysis, 1993-01-01 to 2013-12-31. Distributed by: Gulf of Mexico Research Initiative Information and Data Cooperative (GRIIDC), Harte Research Institute, Texas A&M University Corpus Christi. https://doi.org/10.7266/n7-2zxg-x010

Zhu, Y. (2020b). Daily-mean satellite altimetry measurements from the Gulf of Mexico region, 1993-01-01 to 2017-05-17. Distributed by: Gulf of Mexico Research Initiative Information and Data Cooperative (GRIIDC), Harte Research Institute, Texas A&M University Corpus Christi. https://doi.org/10.7266/n7-ya5j-0t90

Zhu, Y. (2020c). Selected historical mooring data in the Gulf of Mexico from 1997-03-20 to 2014-06-27. Distributed by: Gulf of Mexico Research Initiative Information and Data Cooperative (GRIIDC), Harte Research Institute, Texas A&M University Corpus Christi. https://doi.org/10.7266/n7-7g3d-9q79